Nucleation and arrest of fluid-induced aseismic slip

Antoine B. Jacquey[1] and Robert C. Viesca[1]

[1]Tufts University

December 27, 2022

Abstract

Microseismicity associated with fluid pressurization in the subsurface occurs during fluid injection but can also be triggered after injection shut-in. Understanding the extent and duration of the post-injection microseismicity is critical to limit the risk of fluid-induced seismicity and insure the safe utilization of the subsurface. Using theoretical and numerical techniques, we investigated how aseismic slip on a fault plane evolves and stops after a fluid pressurization event. We found that the locking mechanisms controlling the arrest of aseismic slip highly depend on the initial fault stress criticality and the pressurization duration. The absolute arrest time of fault aseismic slip after injection shut-in is proportional to the pressurization duration and increases significantly with the initial fault stress criticality. Given that microseismicity can be triggered by aseismic slip, these results provide insights into the mechanics controlling the arrest of microseismicity after fluid pressurization as a milestone towards induced seismicity mitigation strategies.

Supporting Information for "Nucleation and arrest of fluid-induced aseismic slip"

Antoine B. Jacquey[1]and Robert C. Viesca[1]

[1]Department of Civil and Environmental Engineering, Tufts University, Medford, MA 02155, USA.

Contents of this file

1. Text S1 to S6
2. Figures S1 to S3
3. Table S1

Introduction

This document contains supporting information on the problem formulation and numerical implementation relevant to the numerical results on fluid-induced seismicity presented in the main article entitled "Nucleation and arrest of fluid-induced aseismic slip". In Text S1, we present the semi-analytical solutions for fluid pressure distribution and evolution during and after injection. Text S2 describes the derivation and discretization of the governing equations for fault slip and opening using the Displacement Discontinuity Method

---

Corresponding author: A. B. Jacquey, Department of Civil and Environmental Engineering, Tufts University, Medford, MA 02155, USA. (antoine.jacquey@tufts.edu)

(derived from the Boundary Element Method). Text S3 presents the elasto-plastic procedure adopted to account for frictional constraints on the fault plane. Text S4 describes the residuals considered in the numerical simulator and the general solution procedure. Text S5 presents a validation of the numerical implementation by comparing the results with a semi-analytical solution. Text S6 introduces Figure S2 showing how the peak slip rate evolves over time after injection shut-in.

Text S1: fluid pressure during and after injection

Fluid pressure is governed by diffusion along the planar fault interface. For a two-dimensional model, fluid pressure is then governed by the following one-dimensional equation:

$$\frac{\partial p}{\partial t} - \alpha \frac{\partial^2 p}{\partial x^2} = 0, \tag{1}$$

where α is the hydraulic diffusivity and x is the direction of the fault interface. Injection is modeled using a constant pressure fluid source at the origin ($x = 0$). With the following initial and boundary conditions:

$$p\left(x, t = 0\right) = p_0, \quad p\left(x = 0, t > 0\right) = p_0 + \Delta p, \tag{2}$$

the known solution for the fluid pressure is:

$$p\left(x, t\right) = p_0 + \Delta p \, \mathrm{erfc}\left(\frac{|x|}{\sqrt{\alpha' t}}\right), \tag{3}$$

where $\alpha' = 4\alpha$ is the nominal hydraulic diffusivity. After injection shut-in (for $t > t_p$), the fluid pressure is free to diffuse and is subject to the following initial conditions (at the end of the pressurization phase):

$$p\left(x, t = t_p\right) = p_0 + \Delta p \operatorname{erfc}\left(\frac{|x|}{\sqrt{\alpha' t_p}}\right). \tag{4}$$

The fluid pressure after injection shut-in can be estimated as the convolution with respect to the spatial variable x of the pressure distribution at $t = t_p$ (Equation 4) and the Green's function (see similar approach by Ciardo and Rinaldi (2022)):

$$p\left(x, t > t_p\right) = p_0 + \frac{\Delta p}{\sqrt{\pi \alpha' \left(t - t_p\right)}} \int_{-\infty}^{+\infty} \operatorname{erfc}\left(\frac{|s|}{\sqrt{\alpha' t_p}}\right) \exp\left(-\frac{|x - s|^2}{\alpha' \left(t - t_p\right)}\right) ds. \tag{5}$$

The convolution in Equation 5 is evaluated numerically using adaptive Gauss-Kronrod quadrature.

Text S2: displacement discontinuity method

For a one-dimensional fault interface, the quasi-static force balance gives the distribution of the normal σ and shear stresses τ respectively as functions of the slip and opening distributions (e.g. Rice et al., 1968):

$$\sigma\left(x, t\right) = \sigma_0 + \frac{\mu'}{\pi} \int_{-a(t)}^{+a(t)} \frac{\partial \epsilon}{\partial s} \frac{1}{s - x} ds, \tag{6}$$

$$\tau\left(x, t\right) = \tau_0 + \frac{\mu'}{\pi} \int_{-a(t)}^{+a(t)} \frac{\partial \delta}{\partial s} \frac{1}{s - x} ds, \tag{7}$$

where ϵ and δ are the fault opening and slip, μ' the effective shear modulus and a the extent of the rupture zone. As we consider a single fault in this study, and because the slip

and opening are by definition zero outside the rupture zone, the integrals in equations 6 and 7 can be evaluated on an arbitrary domain size larger than the rupture size ($L > a$). We discretize the fault segment into n elements and make use of piecewise constant shape functions (e.g. Uenishi & Rice, 2003) to approximate the opening and slip distributions:

$$\epsilon\left(x,t\right) = \sum_{i=1}^{n} \epsilon_i\left(t\right)\varphi_i\left(x\right), \quad \delta\left(x,t\right) = \sum_{i=1}^{n} \delta_i\left(t\right)\varphi_i\left(x\right), \tag{8}$$

where ϵ_i and δ_i are the discretized values of opening and slip and φ_i the shape function in the i^{th} element. For one-dimensional elements, piecewise constant shape functions are expressed as:

$$\varphi_i\left(x\right) = H\left(x - x_i\right) - H\left(x - x_{i+1}\right), \tag{9}$$

where H is the Heaviside step function and x_i and x_{i+1} the limit coordinates of the i^{th} element. Replacing the integral over the entire domain into a sum of integrals over each element, leads to the discretized version of Equations 6 and 7:

$$\sigma_i = \sigma_0 + \sum_{j=1}^{n} \mathbb{E}_{ij}\epsilon_j, \quad \tau_i = \tau_0 + \sum_{j=1}^{n} \mathbb{E}_{ij}\delta_j. \tag{10}$$

$\mathbb{E}_{ij}$ is the elastic collocation matrix expressed as:

$$\mathbb{E}_{ij} = \frac{2\mu' a_j}{\pi\left(\left(\bar{x}_i - \bar{x}_j\right)^2 - a_j^2\right)}, \tag{11}$$

where $a_j = \frac{\Delta x_j}{2}$ is the j^{th} element half-length and $\bar{x}_i$ the coordinate of the i^{th} element centroid. In our implementation (see Text S4), we consider Equations 10 in an incremental

form (over a fixed time step) to compute the increments of normal and shear stresses ($\Delta\sigma$ and $\Delta\tau$) as functions of the increments of opening and slip ($\Delta\epsilon$ and $\Delta\delta$) respectively:

$$\Delta\sigma_i = \sum_{j=1}^{n} \mathbb{E}_{ij}\Delta\epsilon_j, \quad \Delta\tau_i = \sum_{j=1}^{n} \mathbb{E}_{ij}\Delta\delta_j. \tag{12}$$

Text S3: frictional constraints and elasto-plastic approach

As our model aims at understanding the evolution and distribution of stable aseismic slip, we consider a Mohr-Coulomb frictional strength with constant friction coefficient f formulated here as a plastic yield function noted $\mathcal{F}$:

$$\mathcal{F} = \tau - f\,(\sigma - p) \leqslant 0. \tag{13}$$

To account for the constraints imposed by the frictional strength of the fault interface described by Equation 13, we rely on an elasto-plastic splitting for the stress update. We consider the fault surface to be the boundaries of a layer of thickness h. Fault slip and opening are understood to be the difference in displacement between the top and bottom of this layer (see Figure S1). The fault layer can undergo elastic and plastic deformation in response to a given shear and normal stress. The deformation within the layer is described by homogeneous normal and shear strain. Assuming an additive splitting of the shear strain into elastic and plastic parts, the local stresses at a point along the fault surface can be given as:

$$\sigma' = \sigma'_0 + \kappa'\frac{\epsilon}{h}, \quad \tau = \tau_0 + \mu'\,(\gamma - \gamma^p)\,, \tag{14}$$

where κ' is the normal effective modulus, $\sigma' = \sigma - p$ the effective normal stress, $\gamma = \frac{\delta}{h}$ the total shear strain, and γ^p the plastic shear strain. Equation 14 gives a local stress update based on the relative displacement across the layer. The plastic strain is updated following a non-associative (zero dilation) flow rule resulting in plastic deformation only in the shear direction.

The plastic update is done in three steps: (i) first the trial shear stress is computed for a given time step, (ii) the trial yield condition is computed based on the trial shear stress and normal effective pressure, and (iii) the trial shear stress is corrected if yielding occurs. For the k^{th} time step (quantities with subscript (k)), the trial shear stress τ^{tr} is given as:

$$\tau^{tr}_{(k)} = \tau_{(k-1)} + \mu' \Delta\gamma_{(k)}, \tag{15}$$

where $\Delta\gamma_{(k)} = \frac{\Delta\delta_{(k)}}{h}$ is the increment of total shear strain for this time step. With this definition, we can also express the plastic correction from the trial state to obtain the final shear stress when plastic deformation occurs:

$$\tau_{(k)} = \tau^{tr}_{(k)} - \mu' \Delta\gamma^p_{(k)}. \tag{16}$$

The increment of plastic strain is obtained by combining Equations 16 and 13 together as:

$$\Delta\gamma^p_{(k)} = \begin{cases} 0, & \text{if } \tau^{tr}_{(k)} - f\sigma'_{(k)} < 0, \\ \frac{\tau^{tr}_{(k)} - f\sigma'_{(k)}}{\mu'}, & \text{otherwise.} \end{cases} \tag{17}$$

As mentioned in the previous supporting text (Text S2), our implementation is formulated around increment of stresses. We therefore consider Equations 14 in an incremental form as:

$$\Delta\sigma' = \kappa' \frac{\Delta\epsilon}{h}, \quad \Delta\tau = \mu' \left(\Delta\gamma - \Delta\gamma^p\right). \tag{18}$$

Text S4: update procedure

For each time step, we solve for the increments of slip $\Delta\delta$ and of opening $\Delta\epsilon$ given the change in fluid pressure along each element, Δp. The equations governing the increments follow from the combination of Equations 12 and 18:

$$\begin{aligned}
&\sum_{j=1}^{n} \mathbb{E}_{ij}\Delta\epsilon_j - \frac{\kappa'}{h}\Delta\epsilon_i + \Delta p_i = 0, \\
&\sum_{j=1}^{n} \mathbb{E}_{ij}\Delta\delta_j - \frac{\mu'}{h}\left(\Delta\delta_i - h\Delta\gamma_i^p\right) = 0.
\end{aligned} \tag{19}$$

where the subscript i indicates the position of the i^{th} element in the mesh. We denote the left-hand side of these equations the normal and shear residuals, $R_{\epsilon,i}\left(\Delta\epsilon_i\right)$ and $R_{\delta,i}\left(\Delta\epsilon_i, \Delta\delta_i\right)$ respectively. The opening ϵ is governed by elastic deformation within the fault induced by changes in fluid pressure and the slip δ is governed by frictional constraints. Where plastic deformation occurs, the shear residuals depend both on the increments of opening and of slip as Equation 17 can be alternatively expressed when plastic deformation occurs as:

$$\Delta\gamma^p_{(k)} = \frac{\tau_{(k-1)} - f\sigma'_{(k-1)}}{\mu'} + \frac{\Delta\delta_{(k)}}{h} - f\frac{\kappa'}{\mu'}\frac{\Delta\epsilon_{(k)}}{h}. \tag{20}$$

Equations 19 are solved for using Newton-Raphson iterations and a BiCGstab(l) iterative linear solver. The normal effective stress and shear stress are also updated at the end of each time step. At the beginning of each time step, the increments of opening and slip are initialized to zero, and we compute the changes in fluid pressure using the expressions from Text S1. During the first evaluation of the residuals, the shear residuals are equal to zero as the increment of slip is zero and the normal residuals nonzero due to the changes in fluid pressure. In a second iteration, the changes in opening induced by the fluid pressure changes will trigger changes in normal effective stress and therefore plastic deformation where yielding occurs. This, in turn, induces slip on the fault plane. The Newton-Raphson iterations are stopped when the norm of the residuals reaches or is smaller than a given absolute tolerance (1.0×10^{-12} by default). After a successful solve, the cumulative values of opening, slip, normal stress, and shear stress are updated based on the computed increments.

Text S5: verification of the implementation

The implementation of the displacement discontinuity method together with the elasto-plastic correction for frictional constraints have been verified against the analytical solution provided by Viesca (2021) for aseismic slip in response to a constant pressure fluid source.

Figure S2 shows the comparison between the analytical solution of Viesca (2021) and the numerical solution obtained with 10 000 elements. These results were obtained considering a fault stress parameter $T = \left(1 - \frac{\tau_0}{f\sigma'_0}\right) \frac{\sigma'_0}{\Delta p} = 0.5$. The full list of parameter values can be found in Table S1.

Text S6: peak slip rate evolution after injection shut-in

The maximum slip rate after injection shut-in decays over time until becoming null at the arrest time. We demonstrated in the accompanied manuscript that the final arrest time is proportional to the pressurization duration. Here we also show that the peak slip rate scales with the inverse of the square root of the pressurization duration. Furthermore, the evolution of the scaled slip rate is self-similar on time as depicted in Figure S3 as results for three different pressurization durations collapse into one line. However, the slip rate is not self-similar over space in general after injection shut-in.

References

Ciardo, F., & Rinaldi, A. P. (2022). Impact of injection rate ramp-up on nucleation and arrest of dynamic fault slip. *Geomechanics and Geophysics for Geo-Energy and Geo-Resources*, *8*(1), 28. doi: 10.1007/s40948-021-00336-4

Rice, J. R., et al. (1968). Mathematical analysis in the mechanics of fracture. *Fracture: an advanced treatise*, *2*, 191–311.

Uenishi, K., & Rice, J. R. (2003). Universal nucleation length for slip-weakening rupture instability under nonuniform fault loading. *Journal of Geophysical Research: Solid Earth (1978–2012)*, *108*(B1). doi: 10.1029/2001jb001681

Viesca, R. C. (2021). Self-similar fault slip in response to fluid injection. *Journal of Fluid Mechanics*, *928*, A29. doi: 10.1017/jfm.2021.825

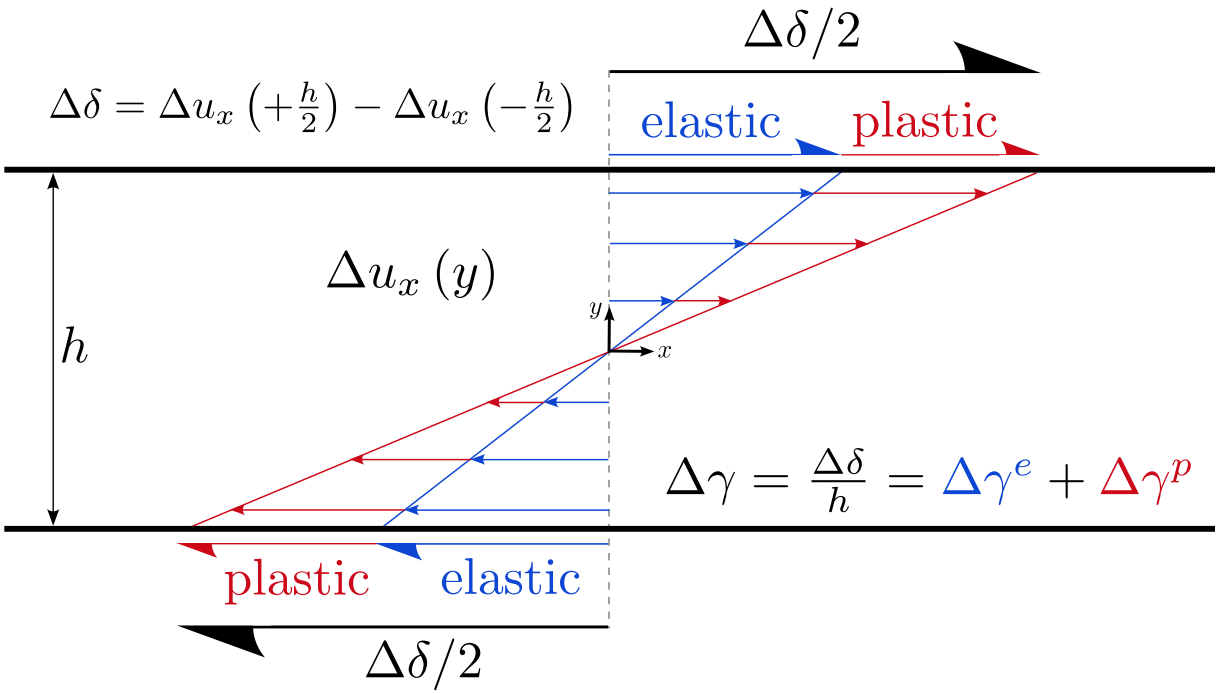

Figure S1. Physical representation of the elasto-plastic splitting of fault shear strain. Slip is defined as the difference in horizontal displacement between the top and bottom of a fault layer of thickness h. The homogeneous shear strain within the layer is split additively into elastic and plastic parts. The magnitude of the elastic strain increment (compared to the plastic one) has been greatly amplified for visual purpose.

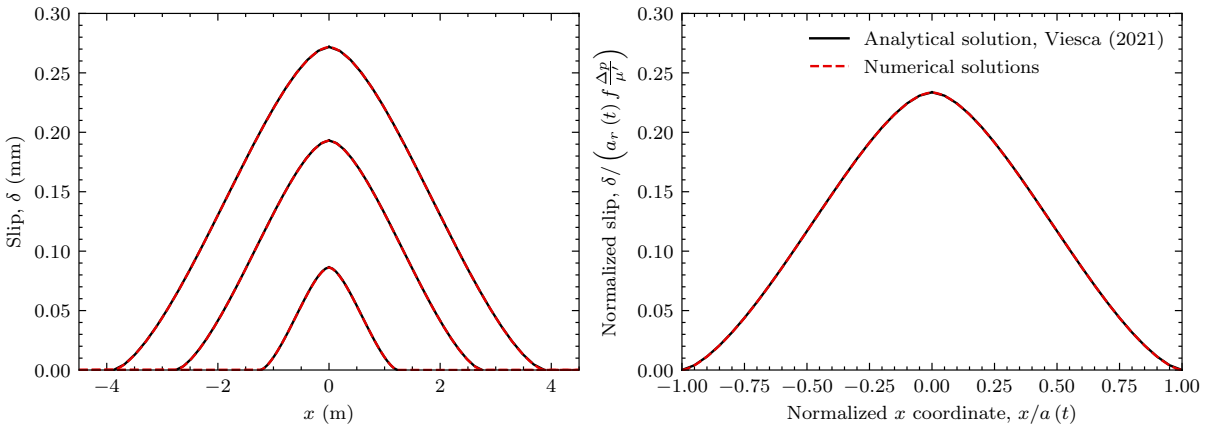

Figure S2. Slip profiles after 1, 5, and 10 mins of pressurization (left) and in its dimensionless form (right) compared with the analytical solution from Viesca (2021).

Table S1. Parameter list for the simulations.

Parameter	Value	Unit
κ'	20	GPa
μ'	20	GPa
h	1	mm
σ_0	50	MPa
p_0	20	MPa
σ'_0	30	MPa
f	0.5	–
Δp	12	MPa
α	0.01	$\mathrm{m\,s^{-2}}$
α'	0.04	$\mathrm{m\,s^{-2}}$

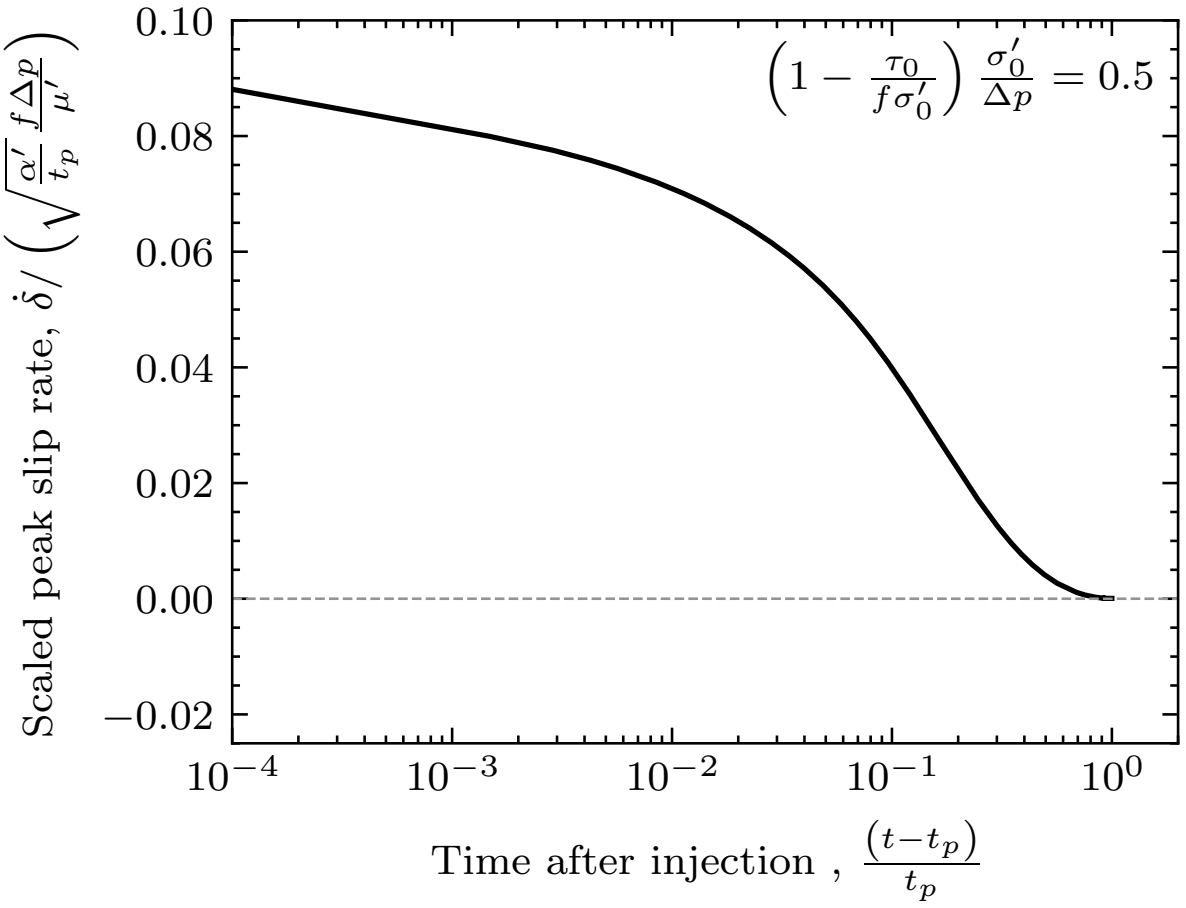

Figure S3. Evolution of the scaled peak slip rate after injection shut-in for three different pressurization durations (collapsed in a single line).

Nucleation and arrest of fluid-induced aseismic slip

Antoine B. Jacquey[1] **and Robert C. Viesca**[1]

[1]Department of Civil and Environmental Engineering, Tufts University, Medford, MA 02155, USA.

Key Points:

- Quantification of fault aseismic slip that continues to propagate away from the former injection point after injection shut-in
- Arrest time of aseismic slip is proportional to the pressurization duration
- Critically stressed faults slip significantly longer and at a greater distance than marginally pressurized faults after injection shut-in

Corresponding author: Antoine B. Jacquey, `antoine.jacquey@tufts.edu`

Abstract

Microseismicity associated with fluid pressurization in the subsurface occurs during fluid injection but can also be triggered after injection shut-in. Understanding the extent and duration of the post-injection microseismicity is critical to limit the risk of fluid-induced seismicity and insure the safe utilization of the subsurface. Using theoretical and numerical techniques, we investigated how aseismic slip on a fault plane evolves and stops after a fluid pressurization event. We found that the locking mechanisms controlling the arrest of aseismic slip highly depend on the initial fault stress criticality and the pressurization duration. The absolute arrest time of fault aseismic slip after injection shut-in is proportional to the pressurization duration and increases significantly with the initial fault stress criticality. Given that microseismicity can be triggered by aseismic slip, these results provide insights into the mechanics controlling the arrest of microseismicity after fluid pressurization as a milestone towards induced seismicity mitigation strategies.

Plain Language Summary

Injection of fluid in the subsurface for energy and storage applications can lead to the onset of microseismicity, and possibly to major induced seismic events. Fluid pressurization decreases the shear strength of surrounding faults and slip occurs when the in-situ shear stress on a fault reaches its shear strength. The nature of slip (aseismic or seismic) depends on the rate at which it occurs and thus on the stability of the deformation. Understanding the mechanics controlling the onset and arrest of aseismic slip and the transition to seismic slip is therefore key to design mitigation strategies for the safe utilization of the subsurface. In this contribution, we investigate using theoretical and numerical techniques how aseismic slip on a fault plane nucleates and evolves in response to fluid injection and how it stops after injection shut-in when fluid pressure relaxes. We demonstrate that critically stressed faults prior to injection can slip for a longer time after injection shut-in than during injection and that the extent of rupture can double in size after the end of injection. These results help to quantify the duration and sphere of influence of fluid injection where microseismicity can occur during and after injection.

1 Introduction

Fluid sources in the subsurface, either natural or anthropogenic, are known to be responsible for the onset of slip on surrounding fault surfaces. Transient natural fluid sources, such as metamorphic dehydration reactions or mantle upwelling, can lead to the migration of generated fluids along fault zones and be responsible for the onset of seismicity swarms, slow slip events, or episodic tremors (Lohman & McGuire, 2007; Roland & McGuire, 2009; Fulton & Saffer, 2009; Fulton et al., 2009; Chen et al., 2012; Shelly et al., 2016; Hatch et al., 2020; Zhu et al., 2020). On the other hand, fluid injection performed in the context of subsurface energy and storage applications can lead to the onset of microseismicity, and to major induced seismic events (Miller et al., 2004; Majer et al., 2007; Ellsworth, 2013; Keranen et al., 2014; Zang et al., 2014; Weingarten et al., 2015; Candela et al., 2018; Goebel & Brodsky, 2018). A mechanistic understanding of the coupling between fluid pressurization and fault slip could therefore have important implications for understanding the influential extent of injection and for mitigating induced seismicity.

Several observations from the laboratory and the field demonstrated that microseismicity and major seismic events are generally preceded by the onset and propagation of aseismic fault slip (Scotti & Cornet, 1994; Guglielmi et al., 2015; Wei et al., 2015; Cappa et al., 2018, 2019). The nucleation of aseismic fault slip due to a fluid source is therefore thought to act as an accompaniment to microseismicity and seismic

slip (Cornet et al., 1997; Ciardo & Lecampion, 2019; Eyre et al., 2019; Garagash, 2021). A number of studies also suggested that aseismic slip plays a major role in controlling the mechanisms responsible for slow slip and episodic tremors (Warren-Smith et al., 2019; Zhu et al., 2020).

Several studies (S. A. Shapiro et al., 1997, 2002; S. Shapiro & Dinske, 2009) investigated how microseismicity migrates in response to fluid injection. Assuming a microseismicity triggering front that propagates at a distance $\sqrt{\alpha t}$, where α is the effective fluid diffusivity and t the time since injection started, these studies aimed at estimating the fluid diffusivity by fitting the triggering front against observations of propagating microseismicity in response to natural and artificial fluid sources (S. A. Shapiro et al., 1997, 2002; S. Shapiro & Dinske, 2009). The underlying assumption in this series of work is that microseismicity is a direct measurement of fluid overpressure migrating. Following the same principles, Parotidis et al. (2004) extended the concept of the triggering front to describe a back front, corresponding to the distance from the injection point at which seismicity is terminated at a given time after stopping fluid injection.

An alternative approach to the fluid-induced seismicity problem is to consider that seismicity is triggered by shear rupture of a network of faults/fractures and not directly by fluid pressure diffusion. By shifting the focus to a fault mechanics process, this implies the existence of a rupture front (mechanically-driven) which is different from the nominal fluid pressure front. Recent studies demonstrated that this concept is mechanically plausible considering a single fault (Aochi et al., 2014; Cappa et al., 2018; Bhattacharya & Viesca, 2019; Viesca, 2021; Sáez et al., 2022) and that it plays a similar role at the scale of the faults/fractures network, including fault stress interactions (Ciardo et al., 2020). In particular, Bhattacharya and Viesca (2019) demonstrated that the relative position of the rupture front with respect to the fluid front is governed by a single quantity being the fault stress parameter capturing the ratio of the fault stress criticality to the amount of pressurization.

While the propagation of aseismic slip in response to fluid injection is now well understood and described in the literature (Bhattacharya & Viesca, 2019; Sáez et al., 2022; Ciardo & Rinaldi, 2022), it remains unclear how aseismic slip evolves after stopping injection or in response to transient injection schedules (Galis et al., 2017; Garagash & Germanovich, 2012). In particular, it is still unknown how far aseismic slip propagates during the post-injection phase, how much additional slip occurs, and how long it takes to the complete locking of the mobilized fault segment. After injection shut-in, fluid pressure decreases around the previous injection point which may lead to a stress re-organization on the fault segment, both of which impacting the fault shear strength. Similarly to the injection problem, the arrest of aseismic slip is likely to be controlled by the changes in shear stress induced by frictional constraints on the fault rather than by fluid diffusion directly. The nature of the coupling between fluid pressure, stress conditions, and aseismic slip arrest remains however unclear for the post-injection phase.

The objective of this study is to understand the processes controlling the arrest of fault aseismic slip after injection shut-in where injection is represented with a constant pressure fluid source. While the onset of injection-induced aseismic slip can be treated analytically or semi-analytically (Viesca, 2021), describing the spatial extent and evolution of aseismic slip after injection shut-in, leading eventually to its arrest is a more challenging problem which can only be treated numerically.

2 Methods

In this study, we performed several numerical experiments of a schematized fault segment of thickness h depicted in Figure 1-b subject to a background stress field

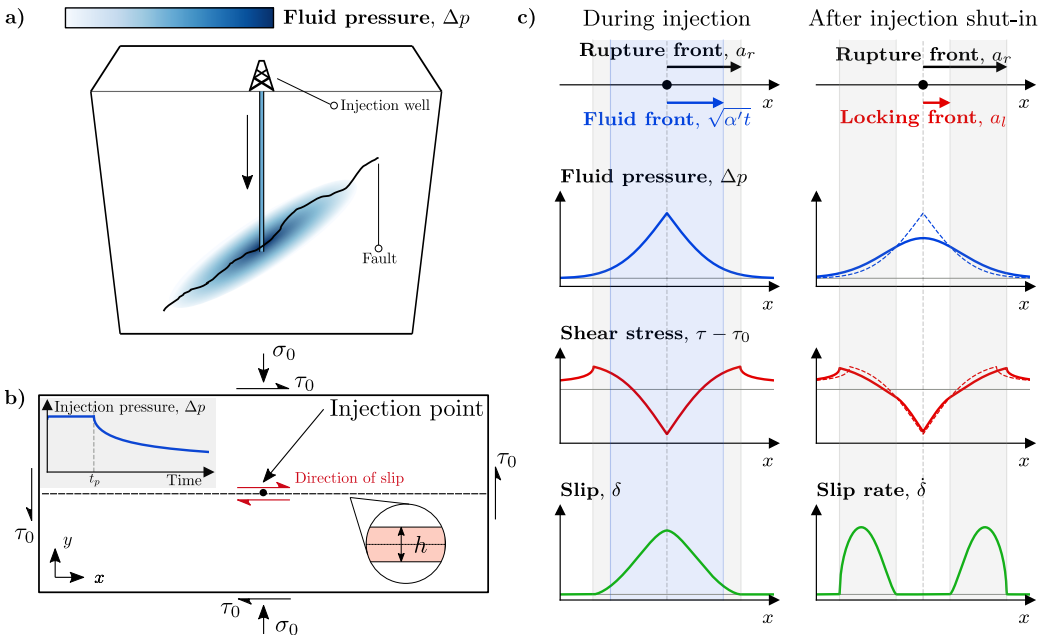

Figure 1. a – Increase in fluid pressure along a fault segment due to fluid injection and associated fault aseismic slip. b – Geometry and boundary conditions for numerical experiments of fluid-induced fault aseismic slip. Evolution over time of the fluid pressure at the injection point is also illustrated. c – Profiles of fluid pressure, shear stress, slip, and slip rate during injection and after injection shut-in obtained numerically.

represented by a normal and shear stress components with respect to the fault plane (along the x axis) noted σ_0 and τ_0 respectively. To account for the possibility of aseismic slip along the fault, its frictional strength τ_s is formulated using a constant Mohr-Coulomb static friction coefficient f:

$$\tau_s = f\,(\sigma - p)\,, \tag{1}$$

where p is the fluid pressure and σ the normal stress (see Supporting Information for details about the slip update). A fluid source is represented by a constant pressure injection point at $x = 0$ which is maintained throughout the pressurization duration (till $t = t_p$). In a recent study, Viesca (2021) demonstrated that for a constant pressure fluid source, the problem of injection-induced aseismic slip reduces to a single parameter, being the fault stress parameter:

$$T = \left(1 - \frac{\tau_0}{f\sigma_0'}\right)\frac{\sigma_0'}{\Delta p}, \tag{2}$$

depending on the pre-injection shear and effective normal stresses τ_0 and σ_0', the friction coefficient f, and the applied overpressure Δp. During the pressurization phase, the slip profiles are self-similar and enlarge with time as $\sim \sqrt{t}$ with the fluid pressure given by:

$$p\,(x,t) = p_0 + \Delta p\,\mathrm{erfc}\left(\frac{|x|}{\sqrt{\alpha' t}}\right). \tag{3}$$

Bhattacharya and Viesca (2019) introduced the aseismic slip front amplification factor λ used as a measure of the relative position of the rupture front a_r with respect to the fluid front $\sqrt{\alpha' t}$ where $\alpha' = 4\alpha$ and α is the hydraulic diffusivity (see Figure 1-c). This front amplification factor depends on the fault stress parameter T, leading to a slip rupture front ahead of the fluid front for critically stressed faults ($T \to 0$) or behind for marginally pressurized faults ($T \to 1$).

After injection shut-in for $t > t_p$, the fluid source is deactivated and the pressure distribution is given (see supplementary material) by:

$$p\left(x, t > t_p\right) = p_0 + \frac{\Delta p}{\sqrt{\pi \alpha' \left(t - t_p\right)}} \int_{-\infty}^{+\infty} \operatorname{erfc}\left(\frac{|s|}{\sqrt{\alpha' t_p}}\right) \exp\left(-\frac{|x-s|^2}{\alpha' \left(t - t_p\right)}\right) ds. \tag{4}$$

This pressure distribution is characterized by a relative drop in fluid pressure around the former injection point together with a slight increase in fluid pressure away from the former injection point, resulting in two symmetrical slipping regions as depicted in Figure 1-c. After injection shut-in, the locking front propagates away from the former injection point and aseismic slip finally arrests when the locking front reaches the rupture front (see Figure 2).

Where aseismic slip occurs on the fault segment, the shear stress equals the fault shear strength. The quasi-static changes in shear stress due to in-plane (mode-II) or anti-plane (mode-III) slip δ can be expressed as (Rice et al., 1968; Uenishi & Rice, 2003):

$$\tau\left(x, t\right) = \tau_0 + \frac{\mu'}{\pi} \int_{-\infty}^{+\infty} \frac{1}{s - x} \frac{\partial \delta}{\partial s}\left(s, t\right) ds, \tag{5}$$

where x is the position along the fault and $\mu' = \frac{\mu}{2(1-\nu)}$ the effective elastic modulus for in-plane (mode-II) case and $\mu' = \frac{\mu}{2}$ for anti-plane (mode-III) case, μ and ν being the shear modulus and the Poisson's ratio respectively. In this study, we discretized Equation 5 using the Displacement Discontinuity Method (DDM) with piecewise constant shape functions (see supplementary materials for details), which allows to express the discretized shear stress as: $\tau = \tau_0 + \mathbb{E} : \delta$, where τ_0 is the initial shear stress and $\mathbb{E}$ is the elastic collocation matrix (dense matrix). Several studies modeled aseismic fault slip using a rate-and-state friction model (Dieterich, 1979; Ruina, 1983) with a slightly velocity strengthening (or slightly velocity weakening and stable) friction coefficient (Rubin, 2008; Dublanchet, 2019; Larochelle et al., 2021; Garagash, 2021; Yang & Dunham, 2021). An alternative to model aseismic slip is to consider the friction coefficient to be constant. This approach implies an unconditionally stable system and provides a simple criterion to account for locked regions on the fault interface where shear stress falls below shear strength. To account for the frictional constraints on the fault plane with a constant friction coefficient, we adopt a local elasto-plastic splitting of the fault slip as described by Sáez et al. (2022), and summarized in the supplementary materials. The results presented here were produced using an in-house implementation (Jacquey, 2022) written with the Julia programming language. Details about the implementation and benchmarking against the analytical solution for constant pressure fluid source (Viesca, 2021) can be found in the supplementary materials.

3 Results

We performed a series of numerical experiments considering different pressurization durations t_p and different values of the fault stress parameter T by varying the initial shear stress acting on the fault plane. Each run consists of a pressurization

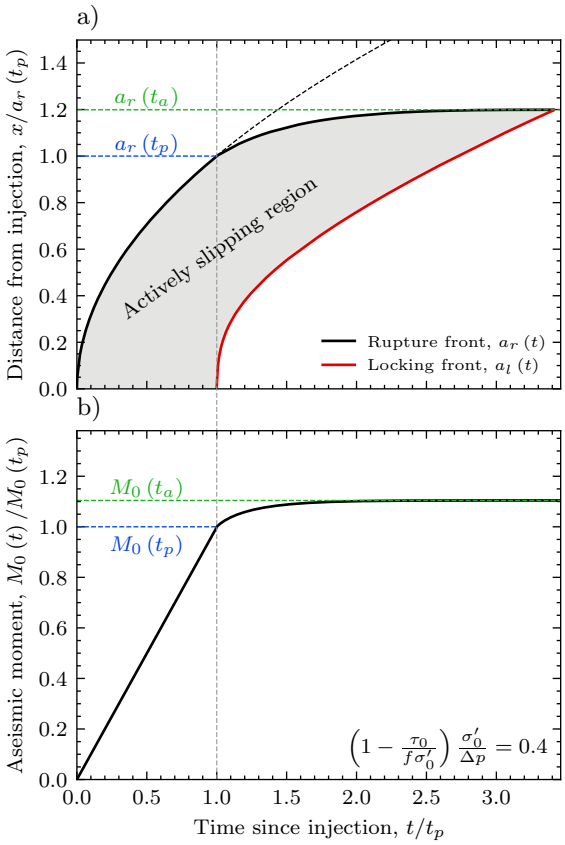

Figure 2. a – Rupture (black solid line) and locking (red solid line) fronts as a function of the time since injection. The black dashed line corresponds to the evolution of the rupture front if injection is maintained. b – Aseismic moment release as a function of the time since injection. These results are obtained using a fault stress parameter $T = \left(1 - \frac{\tau_0}{f\sigma_0'}\right)\frac{\sigma_0'}{\Delta p} = 0.4$.

phase where the constant pressure fluid source is maintained followed by an injection shut-in phase where the injection boundary condition is removed. The simulations are stopped when the entire fault segment is locked and no more slip occurs. In addition to the main quantities describing the system (slip, shear stress, fluid pressure, etc. . .), we kept track of the rupture front (slipping point the farthest form the injection point), the locking front after injection shut-in (slipping point the closest from the former injection point), and the aseismic moment (spatial integral of slip). The results only depend on the fault stress parameter T, as the pressurization duration t_p can be accounted for in the scaling of the temporal quantities. After injection shut-in, the rupture continues to extend farther away from the former injection point, though at a slower pace than if injection was maintained (see Figure 2) while the fault locked region extends from the former injection point until finally reaching the rupture extent. These two fronts delimit the actively slipping region (see gray area in Figure 2) which is maximum at the end of the pressurization phase and decreases in size after injection shut-in. The aseismic moment increases linearly with time during the injection phase. Due to the still actively slipping region, the aseismic moment continues to increase after injection shut-in (see Figure 2). This indicates that a significant amount of microseismicity can still occur after stopping injection and at further distances than reached during the injection phase.

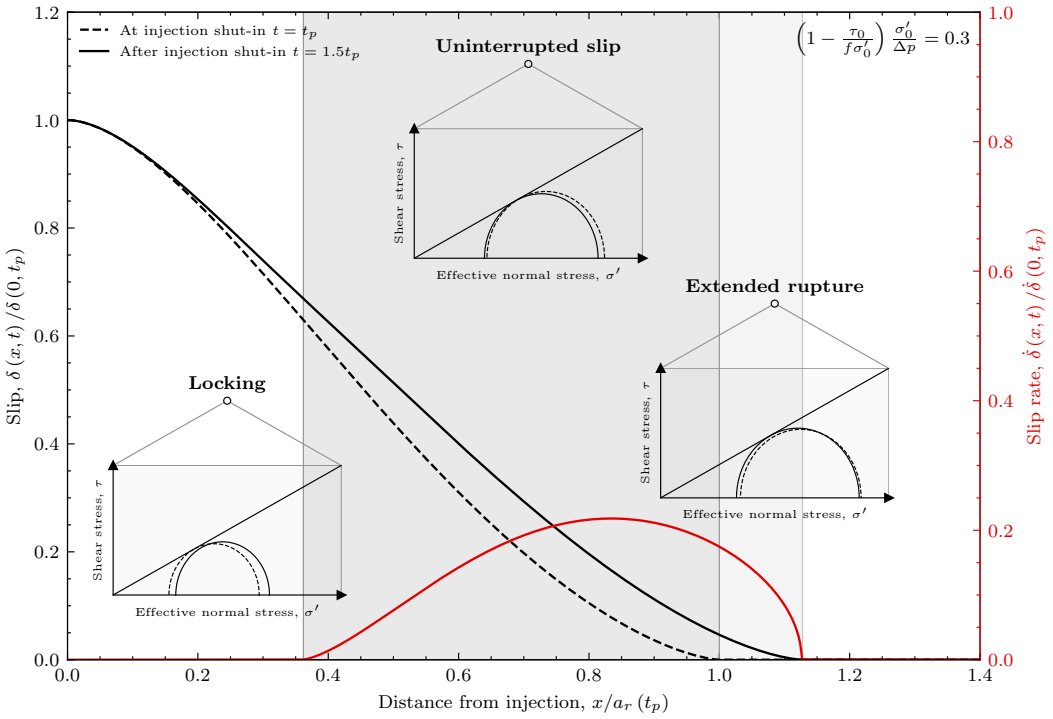

Figure 3. Driving mechanisms for fault aseismic slip after injection shut-in. Red solid line shows the profile of the scaled slip rate after injection shut-in at $t = 1.5 \times t_p$. The black dashed and solid lines correspond to the scaled slip profiles at $t = t_p$ and $t = 1.5 \times t_p$ respectively. The panels show the Mohr-Coulomb diagrams for the three different regimes identified.

After injection shut-in, we identified three regions on the fault segment as depicted in Figure 3. The first one being the locking region around the previous injection point. This region is characterized by a sudden decrease in fluid pressure and associated increase in fault shear strength which leads to the arrest of slip. While the decrease in fluid pressure is the dominant driving mechanisms in this region, we also observed a slight increase in shear stress (see Figure 1-c), indicating that locking is primarily a mechanically-driven mechanism. The size of this region grows over time after injection shut-in until the entire fault segment is locked. The second region refers to an uninterrupted slipping area where slip still occurs after shut-in. A slight increase in fluid pressure due to diffusion (see Equation 4) triggers a stress re-organization associated with a decrease in shear stress. This region is dominated by a stress transfer imposed by the frictional constraints and its size decreases over time. Finally, the third region refers to the newly slipping region where the rupture extended after injection shut-in. The driving mechanism for the new slipping region is similar to the rupture propagation observed during the injection phase. As this region is located near the rupture front, we observed a large increase in shear stress after injection shut-in due to the frictional constraints with peak shear stress values located at the rupture front.

During the pressurization phase, the fault stress parameter T has a significant influence on the mechanical response of the system to injection: Bhattacharya and Viesca (2019) demonstrated that for critically stressed faults ($T \to 0$), the rupture front is far ahead of the fluid front. Our results for the post-injection phase also emphasize the role of the fault stress parameter T on the rate at which slip decays over time after injection shut-in and ultimately on the absolute arrest time of aseismic slip. Given the

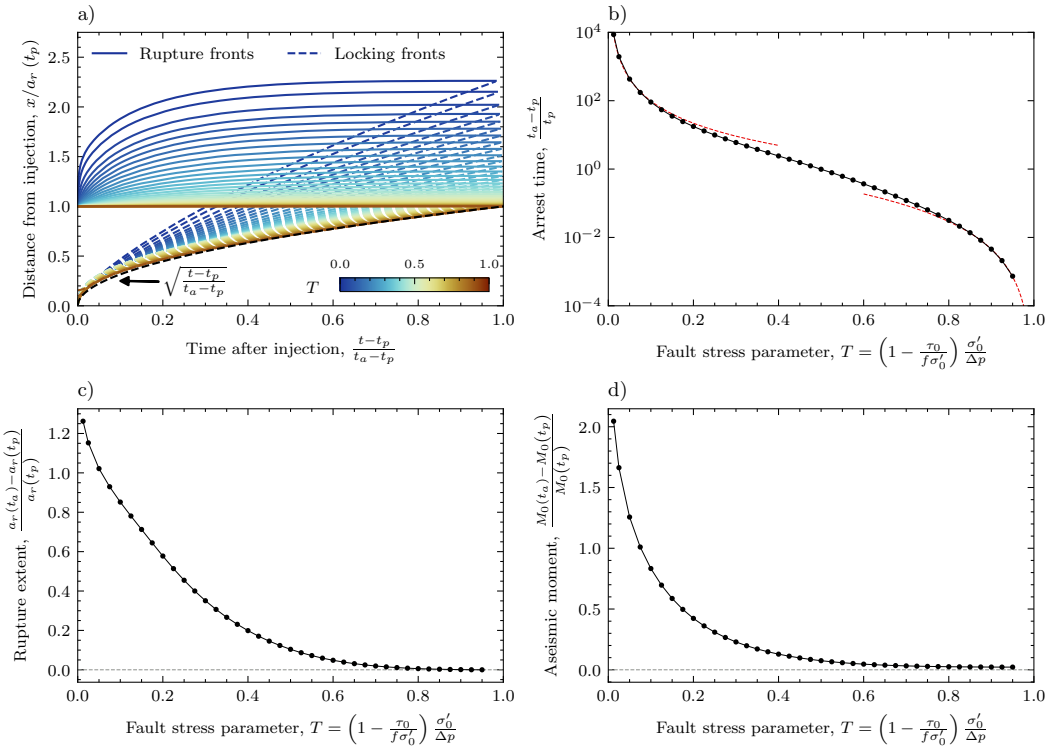

Figure 4. Influence of the fault stress parameter on the rupture and locking fronts evolution (a), the arrest time of aseismic slip (b), final rupture extent (c), and final aseismic moment (d). The red dotted lines in (b) correspond to power law fits at the limits $T \to 0$ and $T \to 1$.

same pressurization duration t_p, critically stressed faults ($T \to 0$) slip aseismically for a significantly longer time (several order of magnitudes) than marginally pressurized faults ($T \to 1$) (see Figure 4-b). The influence of the fault stress parameter is also significant regarding the final rupture extent. The rupture area can increase by more than 50 % for faults with a fault stress parameter of $T \leqslant 0.2$ and double in size for $T \leqslant 0.05$ after injection shut-in (see Figure 4-c). Similar outcomes can be observed for the aseismic moment after injection shut-in. For critically stressed faults ($T \to 0$), the aseismic moment increases by more than 200 % (see Figure 4-d).

After injection shut-in, the evolution of the extent of the actively slipping region strongly depends on the initial fault stress criticality. Figure 4-a shows the evolution of the rupture and locking fronts over time for several values of the fault stress parameter. Considering the same pressurization duration, the locking and rupture fronts scale differently for each value of the fault stress parameter, even though all these realizations share a common fluid pressure evolution. These results indicate that, similarly to the injection case where the rupture front depends not only on the fluid front but also on the fault stress parameter, the locking of the fault after injection shut-in is primarily driven by changes in shear stress imposed by frictional constraints and fluid pressure relaxation. For the limit of marginally pressurized faults ($T \to 1$), the locking front evolution scales with the square root of the scaled time after injection (dashed black line in Figure 4-a), indicating that for this regime, fluid pressure relaxation by diffusion might dominate shear stress changes and therefore control fault locking.

While the self-similarity of slip observed during the injection phase (Viesca, 2021) breaks when injection stops, our dimensional analysis indicates that the pressurization

duration (t_p) and the rupture extent ($a_r\,(t_p)$) are time and spatial scales respectively which control how slip and slip rate distributions evolve over time after injection shut-in. In consequence, the arrest time of aseismic slip is found to be proportional to the pressurization duration and the final rupture extent to be proportional to the rupture extent at the end of the injection phase. The duration of the constant pressure fluid source has therefore impacts on the long-term slipping behavior of the fault, even after stopping injection. The absolute values of slip and slip rate also depends on the pressurization duration as demonstrated in the supplementary materials.

4 Discussion and Conclusion

The results presented in this study demonstrate the importance of the initial fault stress criticality on the post-injection behavior of fault aseismic slip. Our numerical analysis highlighted the role of the coupling between fluid pressure and fault aseismic slip in controlling the locking of the fault after injection shut-in. These insights into the controlling mechanism of aseismic slip arrest can help estimating the extent and duration of microseismicity clouds after injection and improve existing mitigation strategies for fluid injection to minimize the risks of fluid-induced seismicity.

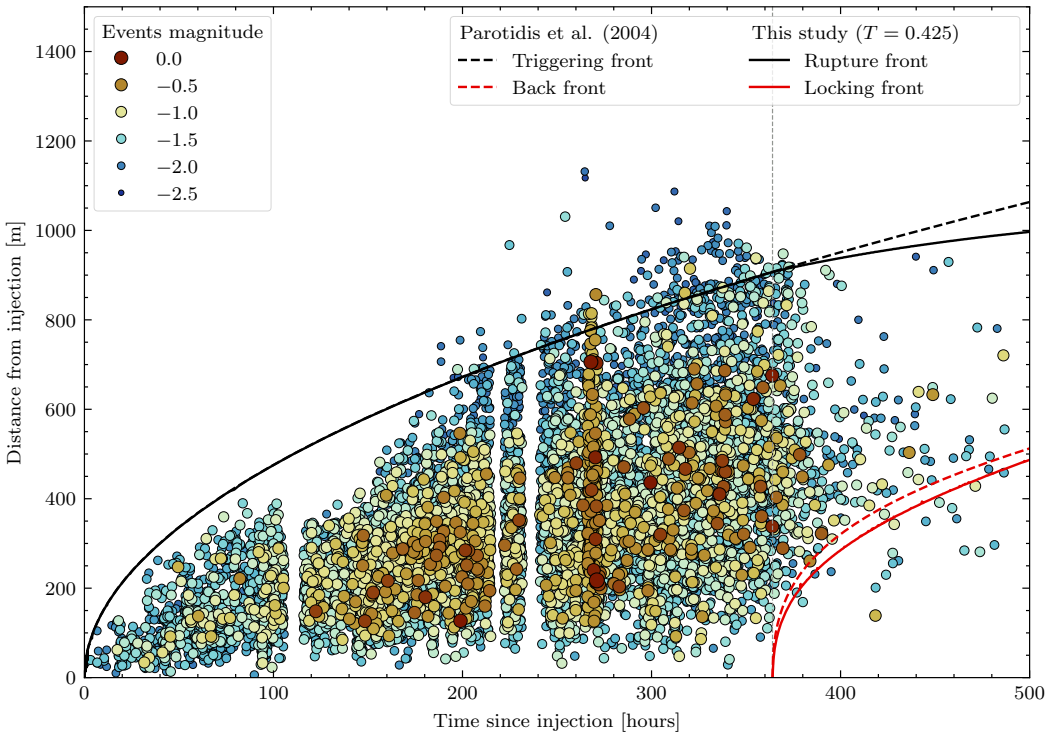

Figure 5. Microseismicity events recorded at Soultz-sous-Forêts (France) during the 1993 hydraulic stimulation of the GPK1 well (EOST and GEIE EMC, 2017; Baria et al., 1996) displayed as their distance from the injection point as a function of the time since the beginning of the stimulation treatment. The size and color of each event correspond to its magnitude. The dashed lines correspond to the triggering and back fronts estimated by Parotidis et al. (2004) based on the diffusion of a fluid pressure point source. The solid lines correspond to the estimation of the rupture and locking fronts following the concepts presented in this study obtained with $T = 0.425$. The vertical gray line corresponds to the interruption of the stimulation and the beginning of the shut-in phase.

Parotidis et al. (2004) investigated the existence and propagation of a back front controlling the arrest of microseismicity events after termination of fluid injection. They proposed that the arrest of microseismicity is governed by the diffusive expansion of a fluid pressure decay following the termination of an overpressure point source and the authors formulated a back front evolution depending on the fluid diffusivity. Using this approach, Parotidis et al. (2004) could indirectly estimate the bulk fluid diffusivity of a fractured rock mass using several catalogs of fluid-induced microseismicity clouds in the field. However, these estimates neglected the impacts of the inelastic deformation occurring in fracture networks on the propagation and arrest of microseismicity. Figure 5 shows such a catalog with the microseismicity recorded in Soultz-sous-Forêts (France) during the hydraulic stimulation of the GPK1 geothermal well in 1993. During the first phase of the stimulation between September 1st and September 17th 1993, approximately 20 000 m^3 of fluid was injected at a depth between 2850 and 3400 m. Moreover, an apparent 10 000 microseismic events were recorded (Cauchie et al., 2020). As an approximation of the volumetric extent stimulated by active aseismic slip, our model predictions of the rupture and locking fronts give satisfying qualitative constraints of the spatio-temporal evolution of these events during the stimulation and after injection shut-in. Our prediction of the rupture and locking fronts share strong similarities with the previously estimated pressurization envelope and back front of Parotidis et al. (2004), indicating that an existence of the two fronts could as well be explained by the cessation of aseismic slip on a fault facture network. This comparative example remains however qualitative as the level of idealization in our conceptual model prevents us from drawing precise estimates of the fault stress parameter or the effective hydraulic diffusivity. A more realistic if computationally intensive representation would be to consider transient fluid injection and migration in a fracture network, rather than on a single fault. This would refine our estimates of the rupture and locking fronts and, in turn, our quantification of the estimate of effective hydraulic diffusivity of the fractured rock mass and of the regional stress field (as resolved on the most critically oriented, conductive faults). An initial step in this direction is the examination of the same phenomenon in mixed mode rupture (Sáez et al., 2022; Sáez & Lecampion, 2022) and in the plane-strain analysis of monotonic injection into a fracture network (Ciardo & Lecampion, 2022).

A number of technologies involved in fluid injection in the subsurface rely on so-called traffic light systems to mitigate the risk of fluid-induced seismicity. The traffic light systems are a set of procedures put in place when a given field observation exceeds a predefined threshold (usually seismic magnitude) which, in turn, adjust the fluid injection schedule (reducing injection pressure or injection flow rate) to reduce the said field observation (Bommer et al., 2015; Hofmann et al., 2018). These procedures usually rely on instantaneous field observations and integrate statistical models combined with geological and geophysical data. Considering a transient injection schedule and a network of faults and fractures could extend the results presented in this study to better predict the duration and the sphere of influence of a transient injection, including the extent of microseismicity and its cessation time after injection shut-in. This is particularly relevant considering that an increase in magnitudes is often observed after injection shut-in (Majer et al., 2007). Another concept which could be tested using this approach is to consider back flow as a potential tool to accelerate locking of slipping fractures and therefore limit the extent of microseismicity after reaching a given magnitude. The results presented in this study are therefore a first step toward integrating physics-based criteria into traffic light system relying on the coupling between fluid flow and fault slip thus improving their reliability.

Our study indicates that the final arrest time of fault aseismic slip after stopping injection depends on how critically stressed the fault is and on how long the fault was pressurized. Our results suggest that the post-injection behavior should not be neglected as faults can slip for a significantly longer time than the pressurization

duration and rupture can extend to large distances. The implications of these findings emphasize the need to account for the post-injection phase when designing traffic light systems for reducing the risk of fluid-induced seismicity and to estimate the time and spatial frame of potential induced events after fluid-injection.

5 Open Research

Data used in Figure 5 are available from the CDGP (CDGP - Data Center for Deep Geothermal Energy) website `https://doi.org/10.25577/SSFS1993`. The modeling results presented in this manuscript were obtained using an in-house software written in the Julia programming language (Jacquey, 2022). More details about the software can be found in the supplementary material and on the repository webpage `https://github.com/ajacquey/DDMFrictionalSlip.jl.git`, including examples of input files.

Acknowledgments
This study was supported by the National Science Foundation (grant number 1653382) and the Southern California Earthquake Center (SCEC award number 22142). The authors acknowledge Paul Segall and an anonymous reviewer for their constructive comments that helped improve the quality of the manuscript.

References

Aochi, H., Poisson, B., Toussaint, R., Rachez, X., & Schmittbuhl, J. (2014). Self-induced seismicity due to fluid circulation along faults. *Geophysical Journal International*, *196*(3), 1544–1563. doi: 10.1093/gji/ggt356

Baria, R., Baumgartner, J., & Gérard, A. (1996). *Extended Summary of the Final Report to EC (DGXII), contract JOU2-CT92-0115.* European Hot Dry Rock Programme 1992-1995.

Bhattacharya, P., & Viesca, R. C. (2019). Fluid-induced aseismic fault slip outpaces pore-fluid migration. *Science*, *364*(6439), 464–468. doi: 10.1126/science.aaw7354

Bommer, J. J., Crowley, H., & Pinho, R. (2015). A risk-mitigation approach to the management of induced seismicity. *Journal of Seismology*, *19*(2), 623–646. doi: 10.1007/s10950-015-9478-z

Candela, T., Wassing, B., Heege, J. t., & Buijze, L. (2018). How earthquakes are induced. *Science*, *360*(6389), 598–600. doi: 10.1126/science.aat2776

Cappa, F., Guglielmi, Y., Nussbaum, C., & Birkholzer, J. (2018). On the Relationship Between Fault Permeability Increases, Induced Stress Perturbation, and the Growth of Aseismic Slip During Fluid Injection. *Geophysical Research Letters*, *45*(20), 11,012–11,020. doi: 10.1029/2018gl080233

Cappa, F., Scuderi, M. M., Collettini, C., Guglielmi, Y., & Avouac, J.-P. (2019). Stabilization of fault slip by fluid injection in the laboratory and in situ. *Science Advances*, *5*(3), eaau4065. doi: 10.1126/sciadv.aau4065

Cauchie, L., Lengliné, O., & Schmittbuhl, J. (2020). Seismic asperity size evolution during fluid injection: case study of the 1993 Soultz-sous-Forêts injection (revised). *Geophysical Journal International*, *221*(2), 968–980. doi: 10.1093/gji/ggaa051

Chen, X., Shearer, P. M., & Abercrombie, R. E. (2012). Spatial migration of earthquakes within seismic clusters in Southern California: Evidence for fluid diffusion. *Journal of Geophysical Research: Solid Earth (1978–2012)*, *117*(B4), n/a–n/a. doi: 10.1029/2011jb008973

Ciardo, F., & Lecampion, B. (2019). Effect of Dilatancy on the Transition From Aseismic to Seismic Slip Due to Fluid Injection in a Fault. *Journal of Geophys-*

ical Research: Solid Earth, *124*(4), 3724–3743. doi: 10.1029/2018jb016636

Ciardo, F., & Lecampion, B. (2022). Injection-induced aseismic slip in tight fractured rocks. *arXiv*. Retrieved from `https://arxiv.org/abs/2212.01050` doi: 10.48550/ARXIV.2212.01050

Ciardo, F., Lecampion, B., Fayard, F., & Chaillat, S. (2020). A fast boundary element based solver for localized inelastic deformations. *International Journal for Numerical Methods in Engineering*, *121*(24), 5696–5718. doi: 10.1002/nme.6520

Ciardo, F., & Rinaldi, A. P. (2022). Impact of injection rate ramp-up on nucleation and arrest of dynamic fault slip. *Geomechanics and Geophysics for Geo-Energy and Geo-Resources*, *8*(1), 28. doi: 10.1007/s40948-021-00336-4

Cornet, F. H., Helm, J., Poitrenaud, H., & Etchecopar, A. (1997). Seismic and Aseismic Slips Induced by Large-scale Fluid Injections. *pure and applied geophysics*, *150*(3-4), 563–583. doi: 10.1007/s000240050093

Dieterich, J. H. (1979). Modeling of rock friction: 1. Experimental results and constitutive equations. *Journal of Geophysical Research: Solid Earth*, *84*(B5), 2161–2168. doi: 10.1029/jb084ib05p02161

Dublanchet, P. (2019). Fluid driven shear cracks on a strengthening rate-and-state frictional fault. *Journal of the Mechanics and Physics of Solids*, *132*, 103672. doi: 10.1016/j.jmps.2019.07.015

Ellsworth, W. L. (2013). Injection-Induced Earthquakes. *Science*, *341*(6142), 1225942–1225942. doi: 10.1126/science.1225942

EOST and GEIE EMC. (2017). *Episode: 1993 stimulation Soultz-sous-Forêts [Collection].* EOST - CDGP. doi: 10.25577/SSFS1993

Eyre, T. S., Eaton, D. W., Garagash, D. I., Zecevic, M., Venieri, M., Weir, R., & Lawton, D. C. (2019). The role of aseismic slip in hydraulic fracturing–induced seismicity. *Science Advances*, *5*(8), eaav7172. doi: 10.1126/sciadv.aav7172

Fulton, P. M., & Saffer, D. M. (2009). Potential role of mantle-derived fluids in weakening the San Andreas Fault. *Journal of Geophysical Research: Solid Earth (1978–2012)*, *114*(B7). doi: 10.1029/2008jb006087

Fulton, P. M., Saffer, D. M., & Bekins, B. A. (2009). A critical evaluation of crustal dehydration as the cause of an overpressured and weak San Andreas Fault. *Earth and Planetary Science Letters*, *284*(3-4), 447–454. doi: 10.1016/j.epsl.2009.05.009

Galis, M., Ampuero, J. P., Mai, P. M., & Cappa, F. (2017). Induced seismicity provides insight into why earthquake ruptures stop. *Science Advances*, *3*(12), eaap7528. doi: 10.1126/sciadv.aap7528

Garagash, D. I. (2021). Fracture mechanics of rate-and-state faults and fluid injection induced slip. *Philosophical Transactions of the Royal Society A*, *379*(2196), 20200129. doi: 10.1098/rsta.2020.0129

Garagash, D. I., & Germanovich, L. N. (2012). Nucleation and arrest of dynamic slip on a pressurized fault. *Journal of Geophysical Research: Solid Earth (1978–2012)*, *117*(B10). doi: 10.1029/2012JB009209

Goebel, T. H. W., & Brodsky, E. E. (2018). The spatial footprint of injection wells in a global compilation of induced earthquake sequences. *Science*, *361*(6405), 899–904. doi: 10.1126/science.aat5449

Guglielmi, Y., Cappa, F., Avouac, J.-P., Henry, P., & Elsworth, D. (2015). Seismicity triggered by fluid injection–induced aseismic slip. *Science*, *348*(6240), 1224–1226. doi: 10.1126/science.aab0476

Hatch, R. L., Abercrombie, R. E., Ruhl, C. J., & Smith, K. D. (2020). Evidence of Aseismic and Fluid-Driven Processes in a Small Complex Seismic Swarm Near Virginia City, Nevada. *Geophysical Research Letters*, *47*(4). doi: 10.1029/2019gl085477

Hofmann, H., Zimmermann, G., Zang, A., & Min, K.-B. (2018). Cyclic soft stimulation (CSS): a new fluid injection protocol and traffic light system to mitigate

seismic risks of hydraulic stimulation treatments. *Geothermal Energy*, *6*(1), 27. doi: 10.1186/s40517-018-0114-3

Jacquey, A. (2022, aug). *ajacquey/DDMFrictionalSlip.jl: v1.0.0.* Zenodo. doi: 10.5281/zenodo.6987094

Keranen, K. M., Weingarten, M., Abers, G. A., Bekins, B. A., & Ge, S. (2014). Sharp increase in central Oklahoma seismicity since 2008 induced by massive wastewater injection. *Science*, *345*(6195), 448–451. doi: 10.1126/science.1255802

Larochelle, S., Lapusta, N., Ampuero, J., & Cappa, F. (2021). Constraining Fault Friction and Stability With Fluid-Injection Field Experiments. *Geophysical Research Letters*, *48*(10). doi: 10.1029/2020gl091188

Lohman, R. B., & McGuire, J. J. (2007). Earthquake swarms driven by aseismic creep in the Salton Trough, California. *Journal of Geophysical Research: Solid Earth (1978–2012)*, *112*(B4). doi: 10.1029/2006jb004596

Majer, E. L., Baria, R., Stark, M., Oates, S., Bommer, J., Smith, B., & Asanuma, H. (2007). Induced seismicity associated with Enhanced Geothermal Systems. *Geothermics*, *36*(3), 185–222. doi: 10.1016/j.geothermics.2007.03.003

Miller, S. A., Collettini, C., Chiaraluce, L., Cocco, M., Barchi, M., & Kaus, B. J. P. (2004). Aftershocks driven by a high-pressure CO2 source at depth. *Nature*, *427*(6976), 724–727. doi: 10.1038/nature02251

Parotidis, M., Shapiro, S. A., & Rothert, E. (2004). Back front of seismicity induced after termination of borehole fluid injection. *Geophysical Research Letters*, *31*(2). doi: 10.1029/2003gl018987

Rice, J. R., et al. (1968). Mathematical analysis in the mechanics of fracture. *Fracture: an advanced treatise*, *2*, 191–311.

Roland, E., & McGuire, J. J. (2009). Earthquake swarms on transform faults. *Geophysical Journal International*, *178*(3), 1677–1690. doi: 10.1111/j.1365-246x.2009.04214.x

Rubin, A. M. (2008). Episodic slow slip events and rate-and-state friction. *Journal of Geophysical Research: Solid Earth (1978–2012)*, *113*(B11). doi: 10.1029/2008jb005642

Ruina, A. (1983). Slip instability and state variable friction laws. *Journal of Geophysical Research: Solid Earth*, *88*(B12), 10359–10370. doi: 10.1029/jb088ib12p10359

Sáez, A., & Lecampion, B. (2022). Post-injection aseismic slip as a mechanism for the delayed triggering of seismicity. *arXiv*. Retrieved from `https://arxiv.org/abs/2211.16803` doi: 10.48550/ARXIV.2211.16803

Sáez, A., Lecampion, B., Bhattacharya, P., & Viesca, R. C. (2022). Three-dimensional fluid-driven stable frictional ruptures. *Journal of the Mechanics and Physics of Solids*, 104754. doi: 10.1016/j.jmps.2021.104754

Scotti, O., & Cornet, F. (1994). In Situ Evidence for fluid-induced aseismic slip events along fault zones. *International Journal of Rock Mechanics and Mining Sciences & Geomechanics Abstracts*, *31*(4), 347–358. doi: 10.1016/0148-9062(94)90902-4

Shapiro, S., & Dinske, C. (2009). Fluid-induced seismicity: Pressure diffusion and hydraulic fracturing. *Geophysical Prospecting*, *57*(2), 301–310. doi: 10.1111/j.1365-2478.2008.00770.x

Shapiro, S. A., Huenges, E., & Borm, G. (1997). Estimating the crust permeability from fluid-injection-induced seismic emission at the KTB site. *Geophysical Journal International*, *131*(2), F15–F18. doi: 10.1111/j.1365-246x.1997.tb01215.x

Shapiro, S. A., Rothert, E., Rath, V., & Rindschwentner, J. (2002). Characterization of fluid transport properties of reservoirs using induced microseismicity. *Geophysics*, *67*(1), 212–220. doi: 10.1190/1.1451597

Shelly, D. R., Ellsworth, W. L., & Hill, D. P. (2016). Fluid-faulting evolution in

high definition: Connecting fault structure and frequency-magnitude variations during the 2014 Long Valley Caldera, California, earthquake swarm. *Journal of Geophysical Research: Solid Earth*, *121*(3), 1776–1795. doi: 10.1002/2015jb012719

Uenishi, K., & Rice, J. R. (2003). Universal nucleation length for slip-weakening rupture instability under nonuniform fault loading. *Journal of Geophysical Research: Solid Earth (1978–2012)*, *108*(B1). doi: 10.1029/2001jb001681

Viesca, R. C. (2021). Self-similar fault slip in response to fluid injection. *Journal of Fluid Mechanics*, *928*, A29. doi: 10.1017/jfm.2021.825

Warren-Smith, E., Fry, B., Wallace, L., Chon, E., Henrys, S., Sheehan, A., ... Lebedev, S. (2019). Episodic stress and fluid pressure cycling in subducting oceanic crust during slow slip. *Nature Geoscience*, *12*(6), 475–481. doi: 10.1038/s41561-019-0367-x

Wei, S., Avouac, J.-P., Hudnut, K. W., Donnellan, A., Parker, J. W., Graves, R. W., ... Eneva, M. (2015). The 2012 Brawley swarm triggered by injection-induced aseismic slip. *Earth and Planetary Science Letters*, *422*, 115–125. doi: 10.1016/j.epsl.2015.03.054

Weingarten, M., Ge, S., Godt, J. W., Bekins, B. A., & Rubinstein, J. L. (2015). High-rate injection is associated with the increase in U.S. mid-continent seismicity. *Science*, *348*(6241), 1336–1340. doi: 10.1126/science.aab1345

Yang, Y., & Dunham, E. M. (2021). Effect of Porosity and Permeability Evolution on Injection-Induced Aseismic Slip. *Journal of Geophysical Research: Solid Earth*, *126*(7). doi: 10.1029/2020jb021258

Zang, A., Oye, V., Jousset, P., Deichmann, N., Gritto, R., McGarr, A., ... Bruhn, D. (2014). Analysis of induced seismicity in geothermal reservoirs – An overview. *Geothermics*, *52*, 6–21. doi: 10.1016/j.geothermics.2014.06.005

Zhu, W., Allison, K. L., Dunham, E. M., & Yang, Y. (2020). Fault valving and pore pressure evolution in simulations of earthquake sequences and aseismic slip. *Nature Communications*, *11*(1), 4833. doi: 10.1038/s41467-020-18598-z